Computers and Structures 178 (2017) 1–16

Contents lists available at ScienceDirect

Computers and Structures

journal homepage: www.elsevier.com/locate/compstruc

A high order local approximation free from linear dependency with quadrilateral mesh as mathematical cover and applications to linear elastic fractures

Dongdong Xu [a,b], Yongtao Yang [b], Hong Zheng [c,*], Aiqing Wu [a]

[a] Key Laboratory of Geotechnical Mechanics and Engineering of Ministry of Water Resources, Yangtze River Scientific Research Institute, Wuhan 430010, China
[b] State Key Laboratory of Geomechanics and Geotechnical Engineering, Institute of Rock and Soil Mechanics, Chinese Academy of Sciences, Wuhan 430071, China
[c] Key Laboratory of Urban Security and Disaster Engineering, Ministry of Education, Beijing University of Technology, Beijing 100124, China

ARTICLE INFO

Article history:
Received 18 November 2015
Accepted 4 October 2016

Keywords:
Partition of unity based methods
Numerical manifold method
Local approximation
Linear dependency issue

ABSTRACT

The numerical manifold method falls into the category of the partition of unity methods. In order to enhance accuracy, high order polynomials can be specified as the local approximations. This, however, would incur rank deficiency of the stiffness matrix. In this study, a local displacement approximation is constructed over a physical patch generated from a four quadrilateral mathematical mesh. All the degrees of freedom are physically meaningful. The stresses are continuous at all nodes, suggesting that no stress polish is required. The proposed approximations have the same accuracy as the first-order polynomials, but no linear dependency inherent in the latter.

1. Introduction

Mechanical properties of the rock mass is determined by the rock blocks and various discontinuous structural planes. Many rock engineering practices have shown that rock mass failure usually starts from the propagation of internal discontinuity, then large deformation and large displacement follow, and finally engineering accidents happen. Thus it is of practical significance to study the whole process of fractured rock mass, including crack initiation, propagation and coalescence, sliding and finally forming the deposits. To this end, many numerical methods have been developed over the decades to solve the fracture problems.

Under the assumption of continuum, the finite element method (FEM) is the most commonly used in treating the discontinuous problems. There are mainly two models including the equivalent continuum model [1] and the joint or interface element model [2]. There still exist some disadvantages in the simulation of the crack problems with FEM: the finite element mesh must be in accordance with the crack; and remeshing is inevitable during the propagation of cracks.

In order to overcome the defects of FEM as mentioned above, the extended finite element method (XFEM) [3] and generalized finite element method (GFEM) [4] have been developed based on the partition of unity method (PUM). XFEM is an alternative to meshing or remeshing crack surfaces in computational fracture mechanics problems due to the concept of discontinuous and asymptotic partition of unity enrichment of the standard finite element approximation spaces [5]. In XFEM, the discontinuity of crack is simulated by introducing the generalized Heaviside functions; in addition, enrichment functions are also included to capture the stress singularity around crack tip more accurately. In principle, XFEM is not dependent on the finite mesh in tracking the crack, so it has been widely used in the crack growth problems [6–8]. But it still has difficulties in treating the large displacement problems. Recently, the strain smoothing technique in the smoothed FEM [9] (SFEM) proposed firstly by Liu is implanted into XFEM, which is not insensitive to mesh distortion and has a lower computational cost [10]. From then on, many successive excellent works have been done, such as the node-based smoothed XFEM (NS-XFEM) [11], extension of the strain smoothing technique to the higher order elements [12], edge-based XFEM (ESm-XFEM) [13] and combination of XFEM with the scaled boundary finite element method (SBFEM) [14]. They are all applied to solve the fracture problems and show good performance. In addition, an adaptive singular edge-based smoothed FEM (sES-FEM) [15] is a good improvement of the SFEM for the fracture problems. The newly developed isogeometric analysis (IGA) [16], which integrates the methods for analysis and Computer Aided Design (CAD) into a unified process, shows a great potential in solving the fracture problems.

* Corresponding author.
E-mail address: hzheng@whrsm.ac.cn (H. Zheng).

http://dx.doi.org/10.1016/j.compstruc.2016.10.001

GFEM is nearly the same as the numerical manifold method (NMM) in essence except for the treatment of fractures and discrete blocks. The latter has been extended for application to rock mechanics problems with large deformation, whereas GFEM still has difficulties in simulating the movements of discrete rock block system [17]. Similarly, GFEM has been developed to simulate the three-dimensional dynamic crack propagation [18] and the branch crack problems [19].

Element-free method (EFM) is another continuum-based method in solving the strong discontinuity problems [20]. In EFM, the pre-processing is very easy even for those complex three-dimensional problems, because it only needs to discretize the problem domain by a group of nodes and the connection between nodes as in FEM is not necessary. The approximation functions can be directly constructed by the discrete nodes, so the mesh dependence is not as serious as in FEM. In treating the crack propagation problems, there are no mesh distortion and no need to remesh, which has greatly reduced the complexity. Similarly the enrichment functions as in XFEM can also be included to improve the accuracy of the stress field around the crack tip. EFM has been greatly extended to the three-dimensional fracture problems, such as a local partition of unity enriched element-free Galerkin method in which crack path continuity can be guaranteed [21], combination of the cohesive zone model [22], extended meshfree method without asymptotic enrichment where Lagrange multiplier field is added along the crack front to close the crack [23], the meshfree method based on the cracking-particle method [24] and new development of crack tracking procedure [25]. Furthermore, a detailed review of meshless methods based on the global weak forms in solid mechanics can be found in Ref. [26]. The shape functions in EFM are generally very complex, so the computation consummation is very large.

Discrete element method (DEM) and discontinuous deformation analysis (DDA) method are the two discontinuum-based methods in solving the fracture problems. DEM is firstly proposed by Cundall to study the mechanical behaviors of discontinuum such as rock mass [27]. DEM is an explicit algorithm which is based on Newton's second law. Rock mass is viewed as a series of rigid or deformable blocks cut by the discontinuities. The contact force model is represented by the tiny penetration between contact couples. DDA [28] proposed by Shi is an implicit method, which is based on the principle of minimum potential energy. Compared with DEM, DDA allows relatively large time steps and the stiffness matrix can be calculated by analytical simplex integration method. Both DEM and DDA allow large deformation, for example, Camones has utilized DEM to simulate crack propagation and coalescence [29]. Similarly, DDA has also been applied in predicting the failure process of the crack [30].

NMM proposed by Shi [31] can solve continuous and discontinuous problems of rock mechanics in a unified way. Recently it has been developed to solve the fourth-order problems [32]. In NMM, a mathematical patch might be cut into some physical patches, on which independent local approximations are defined. As a result, the discontinuity along a crack can be modeled more naturally. A lot of research work has been done, see Refs. [33–37].

It is no doubt that the high-order NMM with higher precision will be more suitable for the crack problems than the 0-order NMM. Here the high-order NMM refers to the first-order (or above) polynomials as the local approximations on the physical patches; while 0-order NMM polynomials means that constants are selected as the local approximations on the physical patches. However, the use of high-order polynomials is suffering from the linear dependence, where the global stiffness matrix is rank deficient even after the rigid body displacement modes are removed. The linear dependency issue is called as a 'nail' problem by its inventor. More details can be found in [38].

In this study, aiming at keeping the high precision and eliminating the linear dependency issue, a new displacement approximation scheme is proposed. Furthermore, the enrichment functions used to capture the singular stress field around crack tips are also included. Then the enhanced NMM is applied to elastic and fracture problems. The linear dependency issue has been resolved.

2. Foundation of numerical manifold method

NMM is based on the two cover systems including the mathematical cover (MC) and the physical cover (PC), so as to solve the continuous and discontinuous problems in a unified way. It should be pointed out that MC and PC are not independent from each other, PC is obtained by cutting MC with the components of the problem domain, including the boundary, the material interface and the discontinuity. Here, MC will be formed from a quadrilateral mathematical mesh.

An MC consists of a finite number of simply connected domains. Each domain is called as a mathematical patch (MP), which, in this study, is the union of several quadrilaterals sharing the same node such as MP-1 and MP-2 in Fig. 1. While deploying the MC, it is not necessary to force MC to be in accordance with the problem domain and it only needs to assure that the MC covers the problem domain completely.

PC is composed of all physical patches. The physical patches are generated by cutting all the mathematical patches, one by one, with the components of the problem domain. From one mathematical patch, therefore, more than one physical patch might be generated, such as PP-1, PP-2 and PP-*i* in Fig. 1.

Since physical patches partially overlap, a physical patch might be partitioned by other physical patch boundaries into disjointed domains. Each of these domains is referred to as a manifold element. As a result, a manifold element is a common domain of several physical patches. As shown in Fig. 1, the quadrilateral *i*-*j*-*m*-*l* with a segment of crack is a manifold element, which is the common region of physical patches PP-*i*, PP-*j*, PP-*m* and PP-*l*. Manifold elements are basic units in the numerical integration of the weak form of the problem.

In Fig. 1, there are two types of physical patches. Most physical patches are simply connected domains containing no crack tip, which are called nonsingular patches, such as PP-1. While a physical patch containing a crack tip is called as a singular patch, such as PP-*i*, in the center of Fig. 1. For different types of physical patches, different local approximations will be constructed as follows. Furthermore, the manifold elements are classified into three types: (1) normal manifold element covered only by nonsingular patches; (2) blending manifold element covered by both singular patches and nonsingular patches; (3) singular manifold element covered only by singular patches.

In addition, more details about NMM can be found in [34].

3. Construction of local approximations

In this section, a local approximation scheme based on the quadrilateral mathematical mesh is proposed by introducing new displacement approximations originating from the quadrilateral plate element [39] in FEM. The manifold element constructed in this way is denoted as Quad-P. The items of approximation functions and their properties are firstly presented. Then it is further extended to solve the linear elastic fracture problems.

3.1. Local displacement approximations on Quad-P

For the sake of completeness, a brief establishment of the Quad-P approximation functions is presented here. Let $\boldsymbol{x} = (x, y)$ be a point in

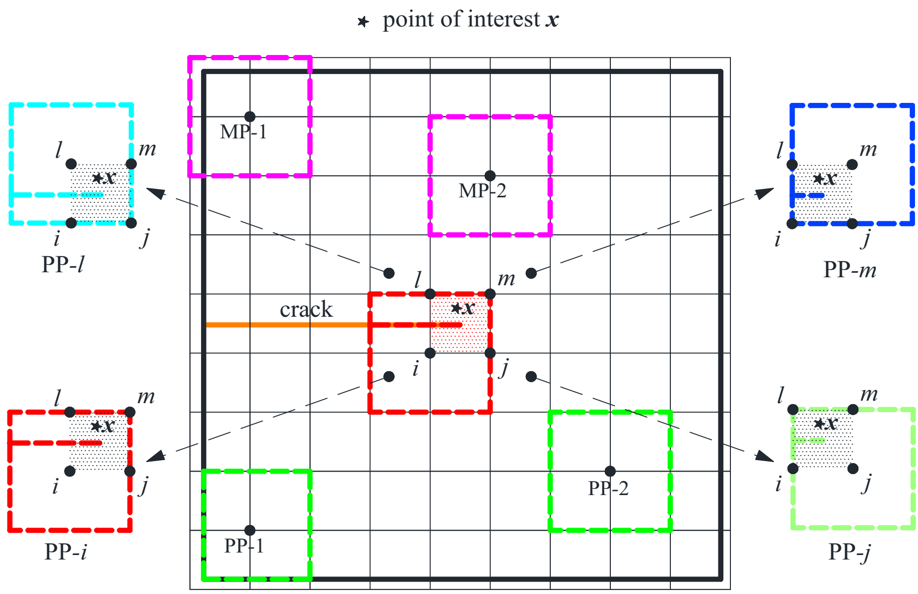

A plate with an edge crack covered by the mathematical cover

Fig. 1. Mathematical patch, mathematical cover, physical patch and physical cover.

a quadrilateral manifold element covered by 4 physical patches denoted as PP-i, PP-j, PP-m and PP-l as schematically sketched in Fig. 1. In the first step, we assume that there is no crack. So the four physical patches are all nonsingular patches. Take PP-i as an example, the horizontal displacement component $u_i(x,y)$ and vertical displacement component $v_i(x,y)$ defined on it can be represented as

$$\begin{cases} u_i(x,y) = N_i(x,y)u^i + N_{ix}(x,y)u^i_y - N_{iy}(x,y)u^i_x \\ v_i(x,y) = N_i(x,y)v^i + N_{ix}(x,y)v^i_y - N_{iy}(x,y)v^i_x \end{cases}, \tag{1}$$

where

$$\begin{cases} N_i = \frac{1}{16}X_1Y_1(X_1Y_1 - X_2Y_2 + 2X_1X_2 + 2Y_1Y_2) \\ N_{ix} = \frac{1}{16}X_1Y_1(2bY_1Y_2) \\ N_{iy} = \frac{1}{16}X_1Y_1(-2aX_1X_2) \end{cases} \tag{2}$$

$$\begin{cases} X_1 = 1 - \frac{x}{a} \\ Y_1 = 1 - \frac{y}{b} \end{cases}, \quad \begin{cases} X_2 = 1 + \frac{x}{a} \\ Y_2 = 1 + \frac{y}{b} \end{cases}, \tag{3}$$

It should be noted that N_{ix} and N_{iy} are not partial derivatives of N_i with respect to x and y. Instead, they are Hermitian interpolation functions associated with $u_i(x,y)$ and $v_i(x,y)$ respectively. In the Eq. (3), a is half of the length between nodal points of PP-i and PP-j or PP-m and PP-l, b is half of the length between nodal points of PP-i and PP-l or PP-j and PP-m.

$$u^i = u(x_i,y_i), u^i_x = \left.\frac{\partial u(x,y)}{\partial x}\right|_{(x_i,y_i)}, \quad \text{and} \quad u^i_y = \left.\frac{\partial u(x,y)}{\partial y}\right|_{(x_i,y_i)}; \tag{4}$$

$$v^i = v(x_i,y_i), v^i_x = \left.\frac{\partial v(x,y)}{\partial x}\right|_{(x_i,y_i)}, \quad \text{and} \quad v^i_y = \left.\frac{\partial v(x,y)}{\partial y}\right|_{(x_i,y_i)}. \tag{5}$$

For elastic problems, under the assumption of small deformation, there are the following relationships between the displacement functions and strain components

$$\frac{\partial u(x,y)}{\partial x} = \varepsilon_x(x,y), \frac{\partial v(x,y)}{\partial y} = \varepsilon_y(x,y); \tag{6}$$

$$\frac{\partial u(x,y)}{\partial y} + \frac{\partial v(x,y)}{\partial x} = \gamma_{xy}(x,y), \ \frac{\partial u(x,y)}{\partial y} - \frac{\partial v(x,y)}{\partial x} = \omega(x,y); \tag{7}$$

where $u(x,y)$ and $v(x,y)$ are the translational displacement components, $\varepsilon_x(x,y)$, $\varepsilon_y(x,y)$ and $\gamma_{xy}(x,y)$ are strain components, $\omega(x,y)$ is rotation angle.

Thus, the following equations are easily derived by solving Eq. (7)

$$\begin{cases} \frac{\partial u(x,y)}{\partial y} = \frac{1}{2}(\gamma_{xy}(x,y) + \omega(x,y)) \\ \frac{\partial v(x,y)}{\partial x} = \frac{1}{2}(\gamma_{xy}(x,y) - \omega(x,y)) \end{cases}. \tag{8}$$

Let

$$\varepsilon^i_x = \varepsilon_x(x_i,y_i), \quad \varepsilon^i_y = \varepsilon_y(x_i,y_i), \tag{9}$$

$$\gamma^i_{xy} = \gamma_{xy}(x_i,y_i), \quad \omega^i = \omega(x_i,y_i), \tag{10}$$

where ε^i_x, ε^i_y and γ^i_{xy} are strain components at the nodal point (x_i,y_i) of physical patch PP-i, ω^i is the corresponding rotation angle.

If $(x,y) = (x_i,y_i)$, Eqs. (6) and (8) can be rewritten as

$$u^i_x = \varepsilon^i_x, \quad v^i_y = \varepsilon^i_y, \tag{11}$$

$$u^i_y = \frac{1}{2}(\gamma^i_{xy} + \omega^i), \quad v^i_x = \frac{1}{2}(\gamma^i_{xy} - \omega^i), \tag{12}$$

Substituting Eqs. (11) and (12) into Eq. (1) and letting $\boldsymbol{u}^i = (u_i(x,y), v_i(x,y))^T$, we have

$$\boldsymbol{u}^i = \boldsymbol{T}^i\boldsymbol{d}_i, \tag{13}$$

where

$$\begin{cases} \boldsymbol{T}^i = \begin{bmatrix} N_i & 0 & -N_{iy} & 0 & \frac{1}{2}N_{ix} & \frac{1}{2}N_{ix} \\ 0 & N_i & 0 & N_{ix} & -\frac{1}{2}N_{iy} & \frac{1}{2}N_{iy} \end{bmatrix}, \\ \boldsymbol{d}^T_i = \begin{pmatrix} u^i & v^i & \varepsilon^i_x & \varepsilon^i_y & \gamma^i_{xy} & \omega^i \end{pmatrix} \end{cases} \tag{14}$$

It is easy to confirm that the above shape functions in Eq. (2) have the following characteristics.

On the nodal point (x_i,y_i) of physical patch PP-i, shape functions have the following properties

$$N_i = \frac{\partial N_{ix}}{\partial y} = -\frac{\partial N_{iy}}{\partial x} = 1, \tag{15}$$

$$N_{ix} = N_{iy} = \frac{\partial N_i}{\partial x} = \frac{\partial N_i}{\partial y} = 0. \quad (16)$$

On the other three nodal points corresponding to physical patches PP-j, PP-m and PP-l; N_i, N_{ix}, N_{iy} and their first-order derivatives are all 0.

The shape functions corresponding to PP-j, PP-m and PP-l which will be given below have the same properties.

For the displacement functions defined on the other three physical patches, we only need to change the index i into j, m or l. The basis functions are as follows

(1) Shape functions of PP-j

$$\begin{cases} N_j = \frac{1}{16}X_2Y_1(X_2Y_1 - X_1Y_2 + 2X_1X_2 + 2Y_1Y_2) \\ N_{jx} = \frac{1}{16}X_2Y_1(2bY_1Y_2) \\ N_{jy} = \frac{1}{16}X_2Y_1(2aX_1X_2) \end{cases}, \quad (17)$$

(2) Shape functions of PP-m

$$\begin{cases} N_m = \frac{1}{16}X_2Y_2(X_2Y_2 - X_1Y_1 + 2X_1X_2 + 2Y_1Y_2) \\ N_{mx} = \frac{1}{16}X_2Y_2(-2bY_1Y_2) \\ N_{my} = \frac{1}{16}X_2Y_2(2aX_1X_2) \end{cases}, \quad (18)$$

(3) Shape functions of PP-l

$$\begin{cases} N_l = \frac{1}{16}X_1Y_2(X_1Y_2 - X_2Y_1 + 2X_1X_2 + 2Y_1Y_2) \\ N_{lx} = \frac{1}{16}X_1Y_2(-2bY_1Y_2) \\ N_{ly} = \frac{1}{16}X_1Y_2(-2aX_1X_2) \end{cases}. \quad (19)$$

To this point, the displacement approximation vector defined on the manifold element can be represented as

$$\boldsymbol{u} = \boldsymbol{u}^i + \boldsymbol{u}^j + \boldsymbol{u}^m + \boldsymbol{u}^l. \quad (20)$$

Figs. 2–4 typically depict the shape functions of Quad-P. As expected, the Quad-P shape functions N_i, N_j, N_m and N_l are very smooth as shown in Fig. 2(a) and (b). The first-order derivatives of the Quad-P shape functions are also sketched in Figs. 3 and 4 respectively, for better observation. Ref. [40] has proposed a so-called extended consecutive-interpolation quadrilateral element (XCQ4), which have good performance even in treating the linear elastic fracture problems. Obviously, the proposed shape functions and the corresponding derivatives of Quad-P behave slightly smoother than those of XCQ4.

3.2. Local displacement approximations on cracked Quad-P

If there is a crack tip in the physical patch PP-i, we still include the additional enriched displacement functions to capture the stress singularity around the crack tip, which can be expressed as

$$\boldsymbol{u}_s^i = N_i \boldsymbol{\Phi}^i \boldsymbol{d}_i^s, \quad (21)$$

where

$$\boldsymbol{\Phi}^i = \begin{bmatrix} \Phi_1 & 0 & \Phi_2 & 0 & \Phi_3 & 0 & \Phi_4 & 0 \\ 0 & \Phi_1 & 0 & \Phi_2 & 0 & \Phi_3 & 0 & \Phi_4 \end{bmatrix}, \quad (22)$$

$$(\Phi_1 \quad \Phi_2 \quad \Phi_3 \quad \Phi_4) = \left(\sqrt{r}\cos\tfrac{\theta}{2} \quad \sqrt{r}\sin\tfrac{\theta}{2} \quad \sqrt{r}\cos\tfrac{3\theta}{2} \quad \sqrt{r}\sin\tfrac{3\theta}{2}\right). \quad (23)$$

(r, θ) is a polar coordinate system with its origin at the crack tip.

Similarly, the singular displacement functions corresponding to other three physical patches can be obtained by replacing the index i by j, m or l.

Therefore, the complete displacement functions of the manifold element is represented as

$$\boldsymbol{u} = \boldsymbol{u}^i + \boldsymbol{u}^j + \boldsymbol{u}^m + \boldsymbol{u}^l + \boldsymbol{u}_s^i + \boldsymbol{u}_s^j + \boldsymbol{u}_s^m + \boldsymbol{u}_s^l \quad (24)$$

4. Discrete equations for Quad-P and integration strategies

In NMM, mathematical cover does not have to be in accordance with the solution domain, so the displacement boundary conditions cannot be applied directly as in FEM. The displacement boundary conditions should be included into the potential energy by the Lagrange multiplier method or the penalty function method. In this study, the penalty function method is adopted, so the potential energy can be expressed as

$$\Pi(\boldsymbol{u}) = \int_\Omega \frac{1}{2}\boldsymbol{\varepsilon}^T\boldsymbol{\sigma}\,\mathrm{d}\Omega - \int_\Omega \boldsymbol{u}^T\boldsymbol{b}\,\mathrm{d}\Omega - \int_{\Gamma_s} \boldsymbol{u}^T\bar{\boldsymbol{p}}\,\mathrm{d}S + \int_{\Gamma_d} \frac{1}{2}\boldsymbol{k}(\boldsymbol{u}-\bar{\boldsymbol{u}})^T(\boldsymbol{u}-\bar{\boldsymbol{u}})\,\mathrm{d}S, \quad (25)$$

where Γ_s is the stress boundary, Γ_d is the displacement boundary, $\bar{\boldsymbol{u}}$ is the given displacement on Γ_d, $\bar{\boldsymbol{p}}$ is the given traction on Γ_s, $\boldsymbol{k}$ is the user-specified penalty.

We will take the singular manifold element as shown in Fig. 1 as an example to introduce the whole derivation process. For the nor-

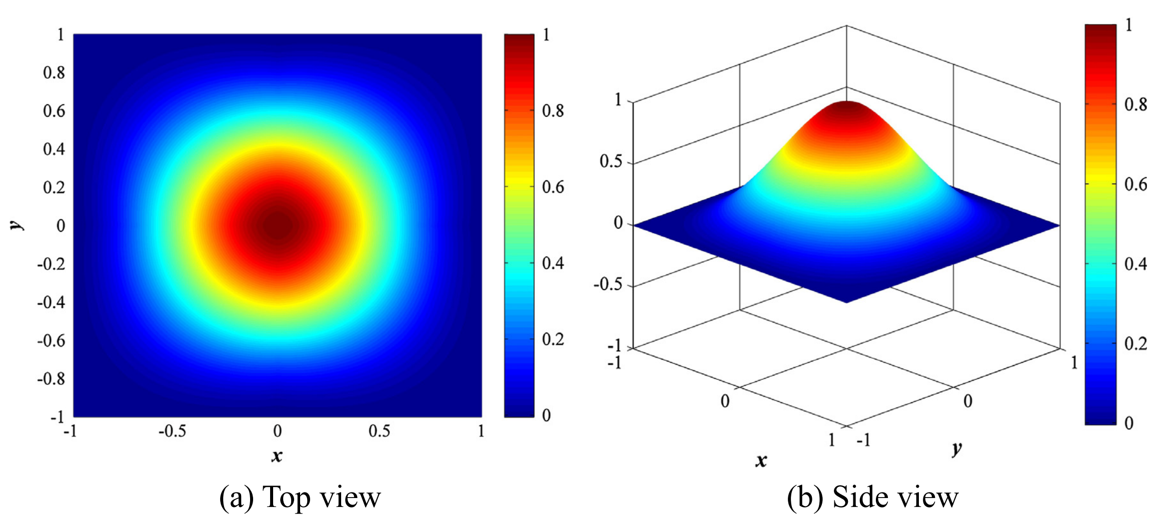

Fig. 2. Nephograms of shape functions N_i, N_j, N_m and N_l.

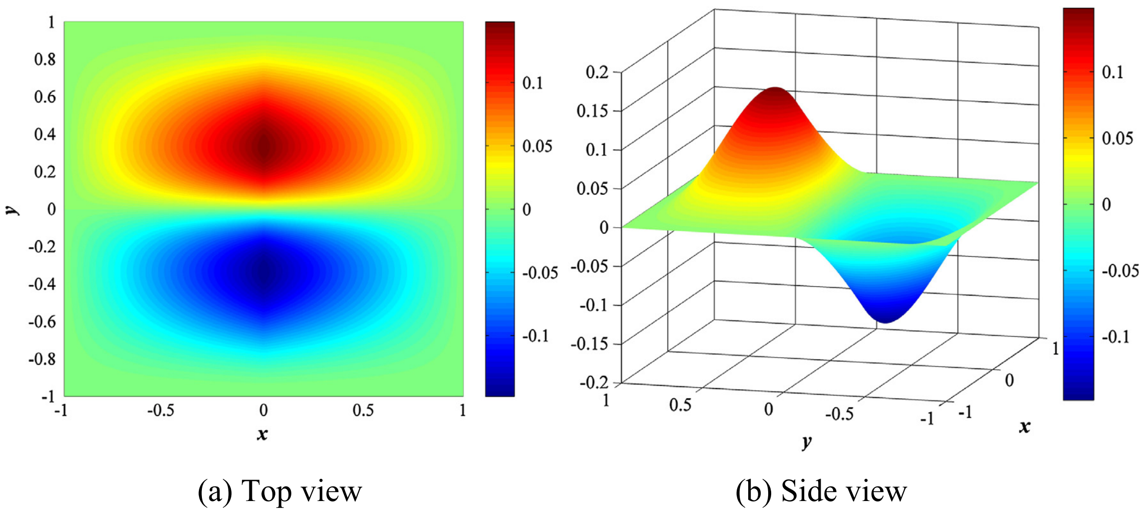

Fig. 3. Nephograms of shape functions N_{ix}, N_{jx}, N_{mx} and N_{lx}.

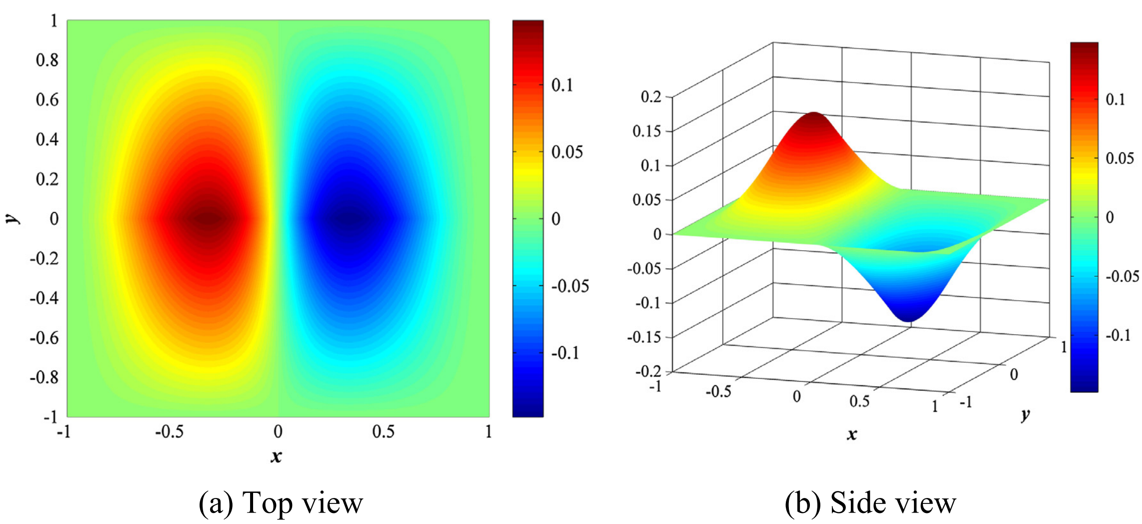

Fig. 4. Nephograms of shape functions N_{iy}, N_{jy}, N_{my} and N_{ly}.

mal or blending manifold elements, we only need to set the corresponding items to zero. Here, the singular manifold element must be covered by 4 singular physical patches denoted as PP-i, PP-j, PP-m and PP-l. Thus, its displacement approximations expressed by Eq. (24) can be rewritten as

$$\boldsymbol{u} = \boldsymbol{N}\boldsymbol{h}, \tag{26}$$

where

$$\boldsymbol{N} = \begin{bmatrix} \boldsymbol{N}^i & \boldsymbol{N}_s^i & \boldsymbol{N}^j & \boldsymbol{N}_s^j & \boldsymbol{N}^m & \boldsymbol{N}_s^m & \boldsymbol{N}^l & \boldsymbol{N}_s^l \end{bmatrix}, \tag{27}$$

$$\boldsymbol{h}^T = \left\{ \boldsymbol{h}_i^T \quad (\boldsymbol{h}_i^s)^T \quad \boldsymbol{h}_j^T \quad \left(\boldsymbol{h}_j^s\right)^T \quad \boldsymbol{h}_m^T \quad (\boldsymbol{h}_m^s)^T \quad \boldsymbol{h}_l^T \quad (\boldsymbol{h}_l^s)^T \right\}. \tag{28}$$

with

$$\boldsymbol{N}^i = \boldsymbol{T}^i, \quad \boldsymbol{h}_i = \boldsymbol{d}_i; \tag{29}$$

$$\boldsymbol{N}_s^i = N_i \boldsymbol{\Phi}^i, \quad \boldsymbol{h}_i^s = \boldsymbol{d}_i^s. \tag{30}$$

The strain ε and displacement u has the following relationship

$$\boldsymbol{\varepsilon} = \boldsymbol{L}_d \boldsymbol{u}, \tag{31}$$

with

$$\boldsymbol{L}_d = \begin{bmatrix} \frac{\partial}{\partial x} & 0 & \frac{\partial}{\partial y} \\ 0 & \frac{\partial}{\partial y} & \frac{\partial}{\partial x} \end{bmatrix}^T. \tag{32}$$

Substituting Eq. (26) into Eq. (31), we have

$$\boldsymbol{\varepsilon} = \boldsymbol{B}\boldsymbol{h}, \tag{33}$$

where

$$\boldsymbol{B} = \begin{bmatrix} \boldsymbol{B}^i & \boldsymbol{B}_s^i & \boldsymbol{B}^j & \boldsymbol{B}_s^j & \boldsymbol{B}^m & \boldsymbol{B}_s^m & \boldsymbol{B}^l & \boldsymbol{B}_s^l \end{bmatrix}, \tag{34}$$

with

$$\boldsymbol{B}^i = \boldsymbol{L}_d \boldsymbol{N}^i, \tag{35}$$

$$\boldsymbol{B}_s^i = \boldsymbol{L}_d \boldsymbol{N}_s^i. \tag{36}$$

The stress $\boldsymbol{\sigma}$ and strain $\boldsymbol{\varepsilon}$ has the relationship as follows

$$\boldsymbol{\sigma} = \boldsymbol{D}\boldsymbol{\varepsilon}, \tag{37}$$

where $\boldsymbol{D}$ is the elastic matrix, for the plane stress problems, expressed as

$$\boldsymbol{D} = \frac{E}{1-v^2}\begin{bmatrix} 1 & v & 0 \\ v & 1 & 0 \\ 0 & 0 & (1-v)/2 \end{bmatrix}; \tag{38}$$

and for the plane strain problems,

$$\boldsymbol{D} = \frac{E(1-v)}{(1+v)(1-2v)}\begin{bmatrix} 1 & v/(1-v) & 0 \\ v/(1-v) & 1 & 0 \\ 0 & 0 & (1-2v)/[2(1-v)] \end{bmatrix}. \tag{39}$$

Substituting Eq. (33) into Eq. (37), we have

$$\boldsymbol{\sigma} = \boldsymbol{S}\boldsymbol{h}, \tag{40}$$

with

$$\boldsymbol{S} = \boldsymbol{D}\boldsymbol{B}. \tag{41}$$

By substituting Eqs. (26), (33) and (40) into Eq. (25), we have the system of linear equilibrium equations as

$$\boldsymbol{K}\boldsymbol{p} = \boldsymbol{q}, \tag{42}$$

where $\boldsymbol{K}$ is the global stiffness matrix, $\boldsymbol{p}$ is the degrees of freedom including normal and enriched items on all the physical patches, $\boldsymbol{q}$ is the generalized force vector dual to $\boldsymbol{p}$. Both $\boldsymbol{K}$ and $\boldsymbol{q}$ are obtained by assembling all the element stiffness matrices $\boldsymbol{K}^e$ and element load vectors $\boldsymbol{q}^e$, defined as

$$\boldsymbol{K}^e = \int_{\Omega^e} \boldsymbol{B}^T\boldsymbol{D}\boldsymbol{B}\,\mathrm{d}\Omega + \boldsymbol{k}\int_{\Gamma_d^e} \boldsymbol{N}^T\boldsymbol{N}\,\mathrm{d}S, \tag{43}$$

$$\boldsymbol{q}^e = \int_{\Omega^e} \boldsymbol{N}^T\boldsymbol{b}\,\mathrm{d}\Omega + \int_{\Gamma_s^e} \boldsymbol{N}^T\bar{\boldsymbol{p}}\,\mathrm{d}S + \boldsymbol{k}\int_{\Gamma_d^e} \boldsymbol{N}^T\bar{\boldsymbol{u}}\,\mathrm{d}S. \tag{44}$$

respectively.

For the three element types, the different integration strategies are adopted. For the normal element, simplex integration or Gaussian integration is adopted; Gaussian integration for the blending

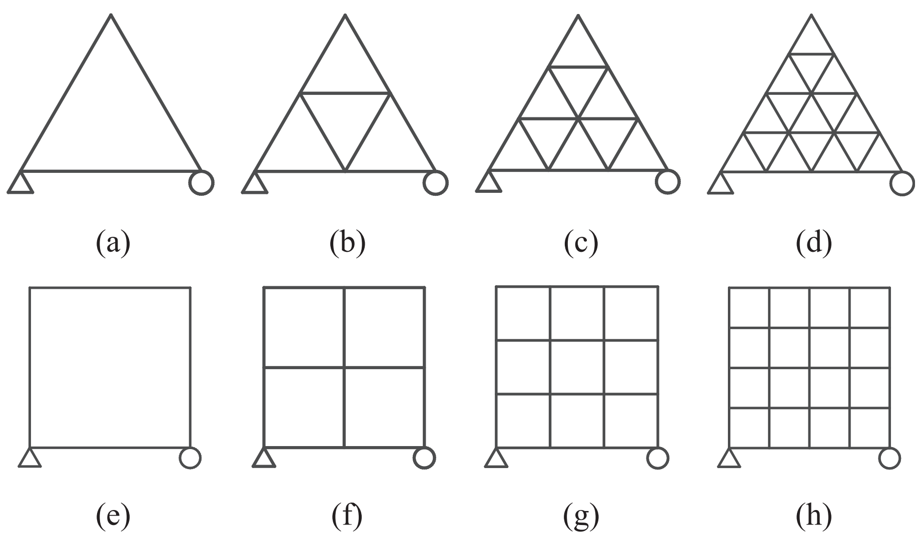

Fig. 5. Meshes for test of linear dependence (Δ - constraints in both *x*- and *y*-direction, O - constraints in the *y*-direction).

Table 1
Comparison of rank deficiency (before constraints).

Element type	1 Element	4 Elements	9 Elements	16 Elements
T3-0	3	3	3	3
T3-1	9	9	9	9
Quad-0	3	3	3	3
Quad-1	11	15	19	23
Quad-P	3	3	3	3

Table 2
Comparison of rank deficiency (after constraints).

Element type	1 element	4 elements	9 elements	16 elements
T3-0	0	0	0	0
T3-1	6	6	6	6
Quad-0	0	0	0	0
Quad-1	8	12	16	20
Quad-P	0	0	0	0

element; for the singular element, the integration scheme in reference [34] is adopted, which can easily treat the $1/r$ singularity of integrand.

5. Demonstration of nodal stress continuity

Taking the partial derivatives of the displacement approximations $\boldsymbol{u}$ with respect to x or y, we have

$$\boldsymbol{u}_{,x} = \boldsymbol{u}^i_{,x} + \boldsymbol{u}^j_{,x} + \boldsymbol{u}^m_{,x} + \boldsymbol{u}^l_{,x} + \boldsymbol{u}^i_{s,x} + \boldsymbol{u}^j_{s,x} + \boldsymbol{u}^m_{s,x} + \boldsymbol{u}^l_{s,x}, \tag{45}$$

$$\boldsymbol{u}_{,y} = \boldsymbol{u}^i_{,y} + \boldsymbol{u}^j_{,y} + \boldsymbol{u}^m_{,y} + \boldsymbol{u}^l_{,y} + \boldsymbol{u}^i_{s,y} + \boldsymbol{u}^j_{s,y} + \boldsymbol{u}^m_{s,y} + \boldsymbol{u}^l_{s,y}, \tag{46}$$

According to the properties of shape functions, it is easy to confirm

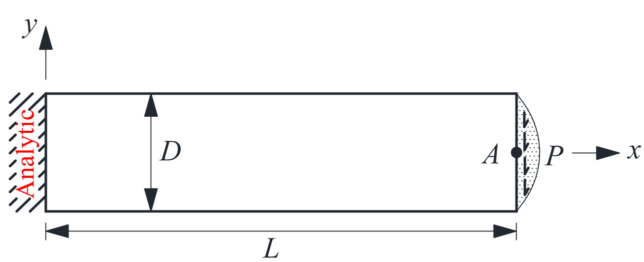

Fig. 6. A 2D cantilever beam subjected to a shear force on the right end.

$$\boldsymbol{u}_{,x}(\boldsymbol{x}_i) = \boldsymbol{u}^i_{,x}(\boldsymbol{x}_i) + \boldsymbol{u}^i_{s,x}(\boldsymbol{x}_i) = \begin{Bmatrix} \varepsilon^i_x \\ \frac{1}{2}\gamma^i_{xy} - \frac{1}{2}\omega^i \end{Bmatrix} + \boldsymbol{\Phi}^i_{,x}\boldsymbol{d}^s_i, \tag{47}$$

$$\boldsymbol{u}_{,y}(\boldsymbol{x}_i) = \boldsymbol{u}^i_{,y}(\boldsymbol{x}_i) + \boldsymbol{u}^i_{s,y}(\boldsymbol{x}_i) = \begin{Bmatrix} \frac{1}{2}\gamma^i_{xy} + \frac{1}{2}\omega^i \\ \varepsilon^i_y \end{Bmatrix} + \boldsymbol{\Phi}^i_{,y}\boldsymbol{d}^s_i. \tag{48}$$

Substituting Eqs. (47) and (48) into Eq. (31), we have

$$\boldsymbol{\varepsilon} = \begin{Bmatrix} \varepsilon^i_x \\ \varepsilon^i_y \\ \gamma^i_{xy} \end{Bmatrix} + \begin{Bmatrix} a_1 \\ a_2 + b_1 \\ b_2 \end{Bmatrix}, \tag{49}$$

where

$$\boldsymbol{\Phi}^i_{,x}\boldsymbol{d}^s_i = \begin{Bmatrix} a_1 \\ a_2 \end{Bmatrix}, \quad \boldsymbol{\Phi}^i_{,y}\boldsymbol{d}^s_i = \begin{Bmatrix} b_1 \\ b_2 \end{Bmatrix}. \tag{50}$$

For a normal manifold element, the second item in Eq. (49) does not exist. So the strain components at the nodal point of PP-*i* is just the third to fifth degrees of freedom on PP-*i*. Consequently, there is no need to solve the strain components at the nodal point by the geometric equations. In addition, the stress components on the nodal point can be directly obtained by multiplying the elastic matrix, which simplifies the calculation greatly.

From Eq. (49), it is easy to see that if several manifold elements share the same physical patch, the stresses at the common nodal point are always equal. In other words, the stresses at the nodal point of physical patch are always continuous. This suggests that no stress polish in the post-processing is necessary. Similarly, an

Table 3
Deflections of point A for tip-shear beam.

Element type	Mesh types					
		Mesh-2	Mesh-4	Mesh-8	Mesh-16	Mesh-32
T3-0	DOFs	26	94	258	758	2834
	M	0.30911	0.71510	0.87768	0.93882	0.97370
T3-1	DOFs	78	282	774	2274	8502
	M	0.99612	0.99938	0.99998	1.00000	1.00000
Quad-0	DOFs	30	90	266	770	2814
	M	0.70966	0.89780	0.97418	0.99322	0.99826
Quad-1	DOFs	90	270	798	2310	8442
	M	0.99831	0.99969	0.99998	1.00000	1.00000
Quad-P	DOFs	90	270	798	2310	8442
	M	1.00000	1.00000	1.00000	1.00000	1.00000
	RD	0	0	0	0	0

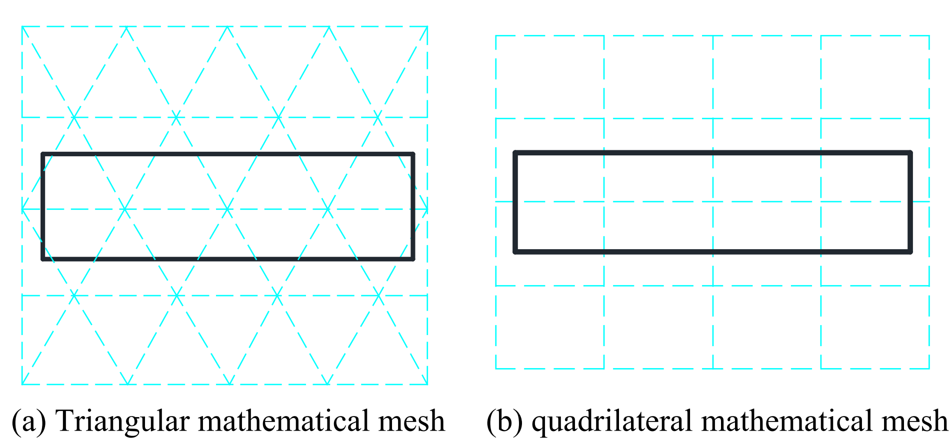

Fig. 7. Mathematical mesh denoted as Mesh-2 for shear beam.

enriched double-interpolation finite element method (XDFEM) [41] also has continuous nodal gradients, smooth nodal stress without post-processing.

6. Numerical tests

Numerical tests with the proposed Quad-P model are carried out, comparing with those by triangular elements and quadrilateral elements based NMM. In the following, T3-0 and T3-1 present the regular triangular mathematical mesh, while the former uses constants as the displacement approximations on the physical patches, and the latter uses the first-order polynomials. Similarly, Quad-0 and Quad-1 represent the quadrilateral mathematical mesh, with the same local approximations as T3-0 and T3-1 respectively.

In this section, the linear dependency tests are first conducted; then four elastic problems are analyzed to verify the solution accuracy of Quad-P; at last the linear elastic fracture problems are solved.

Here, the accuracy of the first four examples below is measured in the form of ratio denoted as M, expressed as

$$M = \frac{R^{\text{num}}}{R^{\text{ref}}} \tag{51}$$

where R^{num} is the numerical result and R^{ref} is the reference solution.

For the last three examples, the stress intensity factors for the mixed-mode cracks are represented as K_{I} and K_{II}, with the accuracy measured in the form of ratio

$$M_{\text{I}} = \frac{K_{\text{I}}^{\text{num}}}{K_{\text{I}}^{\text{ref}}} \tag{52}$$

$$M_{\text{II}} = \frac{K_{\text{II}}^{\text{num}}}{K_{\text{II}}^{\text{ref}}} \tag{53}$$

where $K_{\text{I}}^{\text{num}}$ and $K_{\text{II}}^{\text{num}}$ are the stress intensity factors by numerical simulation, and $K_{\text{I}}^{\text{ref}}$ and $K_{\text{II}}^{\text{ref}}$ are the reference solutions. Here, the stress intensity factors are calculated using the domain forms of interaction integrals [42].

6.1. Linear dependence test

The material parameters in this test include: Young's modulus $E = 1.0$ and Poisson's ratio $\nu = 0.25$. The plane stress condition is assumed. As shown in Fig. 5(a–h), two types of meshes including triangular meshes and quadrilateral meshes with four different mesh densities are adopted to test the linear dependence problem. Comparisons of rank deficiency without and with constraints for the five different cases are shown in Tables 1 and 2. Obviously, for every case in Table 1, it has uniformly three more rank deficiencies than that in Table 2. For T3-0, Quad-0 and Quad-P, the rank deficiencies are all 0 after constraints are enforced, suggesting no linear dependence exists. With the increase in the number of elements, the rank deficiency of T3-1 is always 3 and the rank deficiency of Quad-1 increases.

6.2. Cantilever beam subjected to a tip-shear force

A two-dimensional cantilever beam subjected to a shear force [43] on its right end is studied, as shown in Fig. 6. The parameters in the calculation include: length $L = 48.0$, height $D = 12.0$, shear force $P = 1000.0$, Young's modulus $E = 3.0 \times 10^7$ and Poisson's ratio $\nu = 0.3$. The plane stress condition is assumed. In the calculation, the left boundary of the beam is constrained by the analytical displacements, and the analytical tractions are specified on the right boundary. The exact solution for this case is given by Timoshenko and Goodier [44]

$$u = -\frac{Py}{6EI}\left[(6L-3x)x + (2+\nu)\left(y^2 - \frac{D^2}{4}\right)\right] \tag{54}$$

$$v = \frac{P}{6EI}\left[3\nu y^2(L-x) + (4+5\nu)\frac{D^2 x}{4} + (3L-x)x^2\right] \tag{55}$$

$$\sigma_x(x,y) = -\frac{P(L-x)y}{I} \tag{56}$$

$$\sigma_y(x,y) = 0 \tag{57}$$

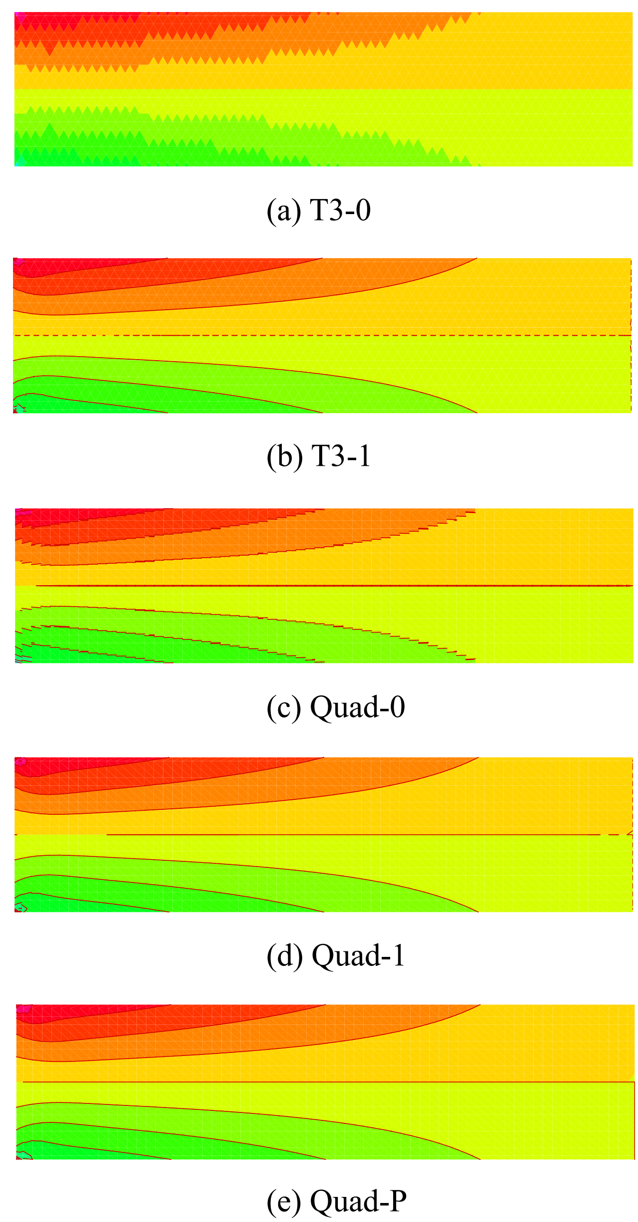

Fig. 8. Contour plots of σ_x for cantilever beam subjected to a tip-shear force for five element types.

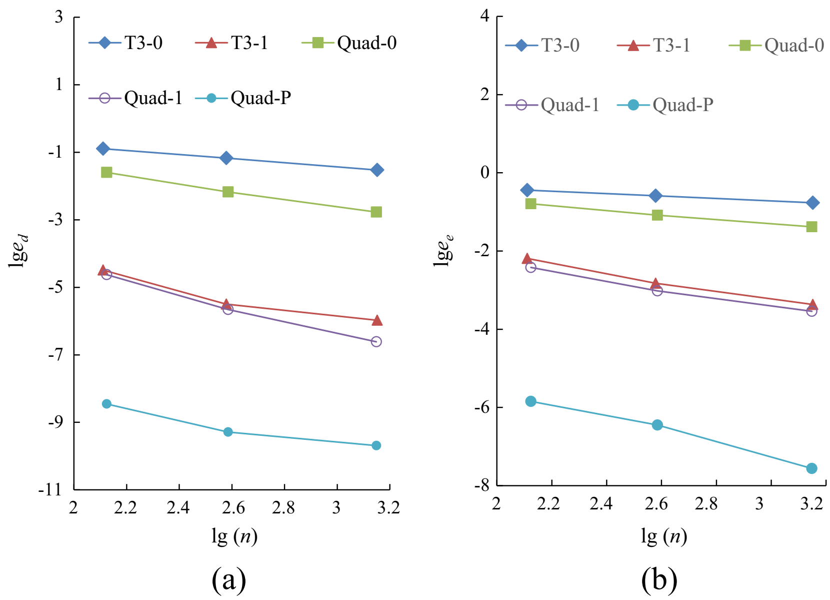

Fig. 9. Comparison of accuracy for cantilever beam problem subjected to a tip-shear force. (a) Relative error in displacement norm; (b) relative error in energy norm.

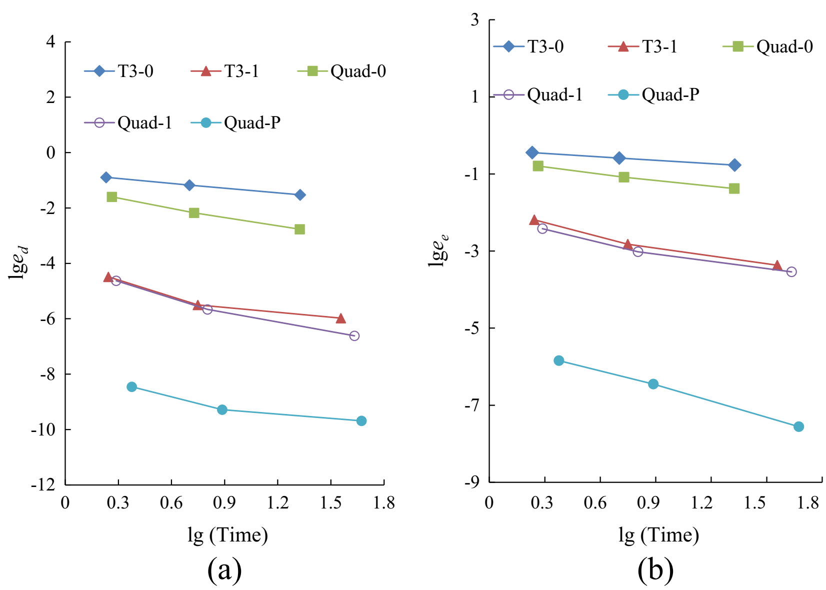

Fig. 10. Computational efficiency assessment for the cantilever beam subjected to a tip-shear force. (a) Relative error in displacement norm; (b) relative error in energy norm.

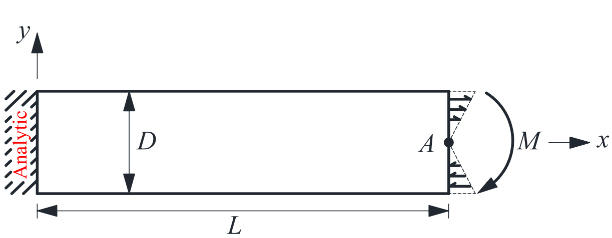

Fig. 11. A cantilever beam subjected to an end-moment.

$$\sigma_{xy}(x,y) = -\frac{P}{2I}\left[\frac{D^2}{4} - y^2\right] \tag{58}$$

where I is the inertia moment and can be expressed as $I = \frac{D^3}{12}$.

The deflection of point A in the form of ratio K is given in Table 3. Five mathematical meshes of different density are designed for this example, among which Mesh-2 means that in the y-direction two element layers are used to cover half of the section; in other words, the beam is covered by four element layers. However, none of the five meshes is in accordance with the beam. Shown in Fig. 7 (a) and (b) are the configurations of Mesh-2 with triangular and quadrilateral meshes.

Deflections of point A under tip-shear force are shown in Table 3. It should be noted that degrees of freedom is abbreviated to DOFs and RD is the abbreviation of rank deficiency. For T3-0 and Quad-0, they both have low precisions when the mesh density is low or says the DOFs are less, although they converge to the analytical solution with the increase in mesh density. For T3-1 and Quad-1, they both have high precisions even if the mesh density

Table 4
Deflections of point A for end-moment beam.

Element type	Mesh types					
		Mesh-2	Mesh-4	Mesh-8	Mesh-16	Mesh-32
T3-0	DOFs	26	94	258	758	2834
	M	0.32095	0.72571	0.88839	0.94944	0.97975
T3-1	DOFs	78	282	774	2274	8502
	M	1.00000	1.00000	1.00000	1.00000	1.00000
Quad-0	DOFs	30	90	266	770	2814
	M	0.707254	0.89505	0.97454	0.99341	0.99832
Quad-1	DOFs	90	270	798	2310	8442
	M	1.00000	1.00000	1.00000	1.00000	1.00000
Quad-P	DOFs	90	270	798	2310	8442
	M	1.00000	1.00000	1.00000	1.00000	1.00000
	RD	0	0	0	0	0

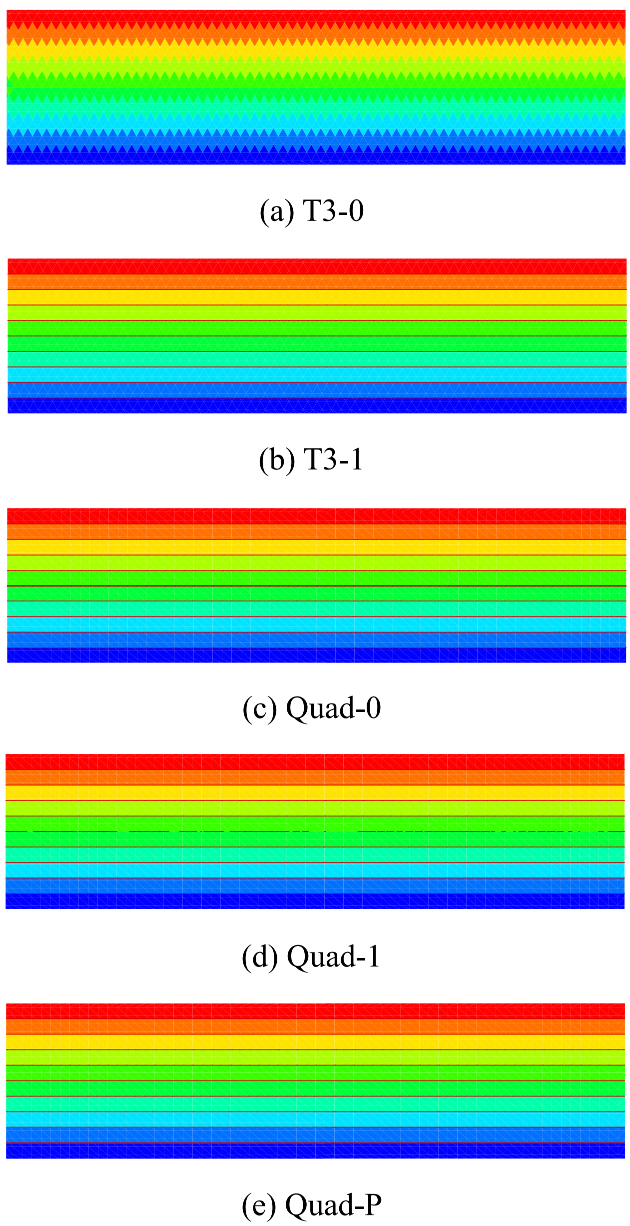

Fig. 12. Contour plots of σ_x for cantilever beam subjected to end-moment for five element types.

is low. Both Quad-1 and the proposed Quad-P have high precisions, but Quad-P is free from linear dependence because the RD is 0.

Contour plots of horizontal stress σ_x for the beam for five element types are shown in Fig. 8(a)–(e). It is found that the stress filed of Quad-P is smoother than others and closer to the exact solution. The contour plots of T3-0 are very coarse because all elements in T3-0 are constant strain elements.

6.2.1. Convergence study

To assess accuracy and convergence, the relative L^2 errors in the displacement norm e_d and the energy norm e_e are defined respectively as follows:

$$e_d = \sqrt{\frac{\int_\Omega (\boldsymbol{u}^{\text{ex}} - \boldsymbol{u}^{\text{num}})^2 d\Omega}{\int_\Omega (\boldsymbol{u}^{\text{ex}})^2 d\Omega}} \tag{59}$$

$$e_e = \sqrt{\frac{\frac{1}{2}\int_\Omega (\boldsymbol{\varepsilon}^{\text{ex}} - \boldsymbol{\varepsilon}^{\text{num}})^{\mathrm{T}} \mathbf{D} (\varepsilon^{\text{ex}} - \boldsymbol{\varepsilon}^{\text{num}}) d\Omega}{\frac{1}{2}\int_\Omega (\boldsymbol{\varepsilon}^{\text{ex}})^{\mathrm{T}} \mathbf{D} (\boldsymbol{\varepsilon}^{\text{ex}}) d\Omega}} \tag{60}$$

where the superscript “ex” represents the exact or analytical solution and the superscript “num” denotes a numerical solution.

Convergence study of numerical solutions for the five element types are conducted. The convergence curves are plotted in Fig. 9. The accuracies of the five element types in both displacement norm and energy norm are compared with each other. From the comparison, it can be seen that Quad-P has the same convergence rate as the other four element types.

6.2.2. Computational efficiency

As in Fig. 9, the proposed Quad-P is indeed able to improve accuracy, at the price of increase in the bandwidth of global stiffness matrix. This will lead to the increase in computational time. Thereby it is necessary to find the right balance between the accuracy and computational speed.

The relative errors in both displacement norm and energy norm versus the corresponding computational time for the five element types are shown in Fig. 10. Quad-P yields more accurate results than the other element types under the same computational time. So the present Quad-P is viewed as computationally more efficient.

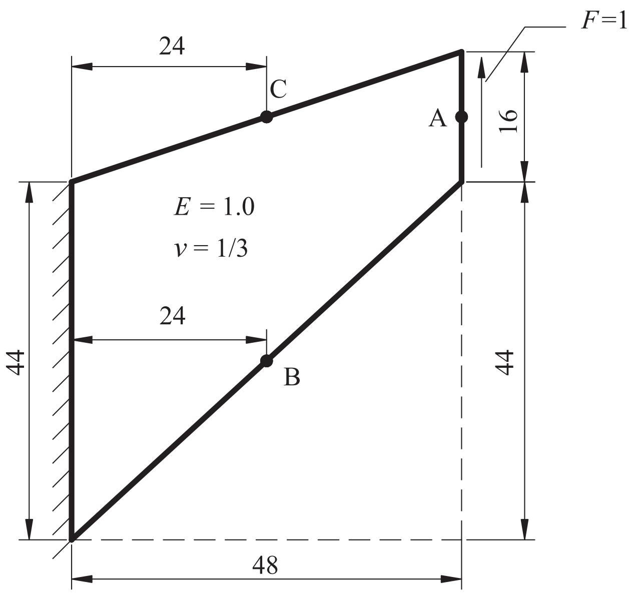

Fig. 13. Cook skew beam subjected to a uniformly distributed shear force.

6.3. Cantilever beam subjected to an end-moment

A cantilever beam subjected to a moment at the right end as in Fig. 11 is considered. The bending moment $M = 24,000$ and other details are the same as that in Section 6.2. The exact solution to this problem is given by Timoshenko and Goodier [44]

$$u = \frac{M}{EI}xy \tag{61}$$

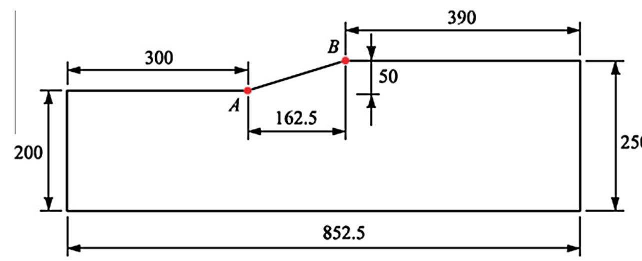

Fig. 14. Dimensions of slope model.

Table 5
Major principal stress at the point *B* for Cook's skew beam.

Element type	Mesh types					
		Mesh-2	Mesh-4	Mesh-8	Mesh-16	Mesh-32
T3-0	DOFs	32	74	242	766	2688
	M	0.5036	0.6549	0.9050	0.9683	0.9934
T3-1	DOFs	96	222	726	2298	8064
	M	0.8699	0.9566	1.0103	1.0046	1.0032
Quad-0	DOFs	42	92	270	818	2790
	M	0.4548	0.6157	0.8126	0.9128	0.9643
Quad-1	DOFs	126	276	810	2454	8370
	M	0.9551	0.9719	0.9951	1.0009	1.0024
Quad-P	DOFs	126	276	810	2454	8370
	M	0.9708	0.9991	1.0025	1.0027	1.0028
	RD	0	0	0	0	0

Table 6
Minor principal stress at the point *C* for Cook's skew beam.

Element type	Mesh types				
	Mesh-2	Mesh-4	Mesh-8	Mesh-16	Mesh-32
T3-0	0.4461	0.8074	0.8913	1.0063	0.9859
T3-1	1.0107	1.0072	1.0033	1.0063	1.0058
Quad-0	1.2415	1.1263	1.1417	1.0673	1.0481
Quad-1	1.0088	1.0159	1.0049	1.0061	1.0060
Quad-P	1.0767	0.9978	1.0056	1.0059	1.0060

Table 7
Vertical displacements at point *A* for Cook's skew beam.

Element type	Mesh types				
	Mesh-2	Mesh-4	Mesh-8	Mesh-16	Mesh-32
T3-0	0.4836	0.7517	0.9162	0.9608	0.9838
T3-1	0.9366	0.9844	0.9977	0.9991	0.9997
Quad-0	0.7127	0.8946	0.9709	0.9918	0.9979
Quad-1	0.9934	0.9972	0.9996	0.9998	1.0001
Quad-P	0.9930	0.9970	0.9993	0.9997	1.0001

Table 8
Horizontal displacements of measured point B for slope.

Element type	Mesh types					
		Mesh-2	Mesh-4	Mesh-8	Mesh-16	Mesh-32
T3-0	DOFs	26	86	242	828	3070
	M	0.5097	0.8432	0.9423	0.9587	0.9931
T3-1	DOFs	78	258	726	2484	9210
	M	1.1051	0.9768	0.9972	0.9984	0.9986
Quad-0	DOFs	30	84	252	850	3056
	M	1.5599	1.1296	1.0693	1.0156	1.0052
Quad-1	DOFs	90	252	756	2550	9168
	M	0.9957	0.9933	1.0001	0.9982	0.9986
Quad-P	DOFs	90	252	756	2550	9168
	M	1.0717	1.0037	1.0012	0.9990	0.9986
	RD	0	0	0	0	0

Table 9
Vertical displacements of measured point A for slope.

Element type	Mesh types				
	Mesh-2	Mesh-4	Mesh-8	Mesh-16	Mesh-32
T3-0	1.2776	1.1390	1.0855	1.0260	1.0029
T3-1	1.1222	1.0206	1.0040	1.0007	1.0001
Quad-0	1.1620	1.0466	1.0303	1.0067	1.0025
Quad-1	1.0591	1.0080	1.0020	1.0004	1.0001
Quad-P	1.0499	1.0079	1.0020	1.0002	0.9999

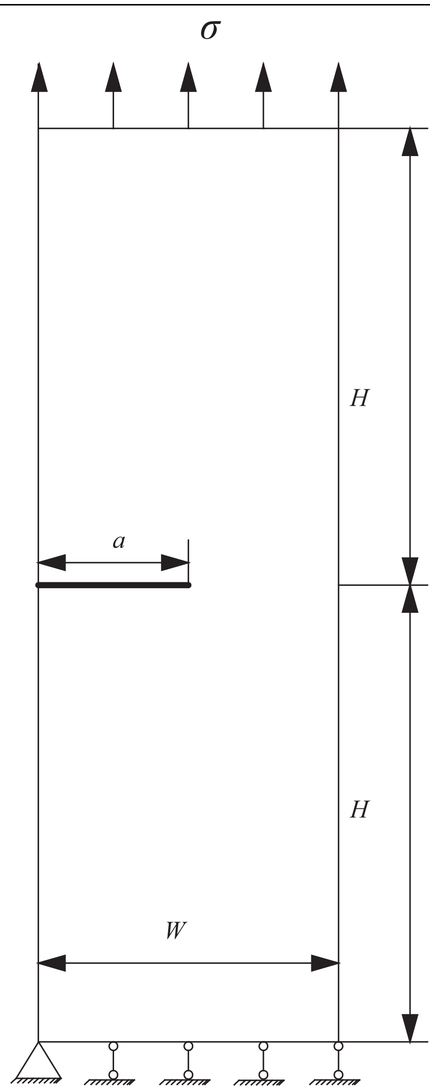

Fig. 15. A finite plate with an edge crack subjected to a uniform tensile force.

$$v = -\frac{vM}{2EI}y^2 - \frac{M}{2EI}x^2 \quad (62)$$

$$\sigma_x = \frac{M}{I}y \quad (63)$$

$$\sigma_y = \sigma_{xy} = 0 \quad (64)$$

Deflection of point A is given in Table 4. Variations of deflection for T3-0 and Quad-0 are the same as the above end-shear case. T3-1, Quad-1 and Quad-P have nearly the same precision with each other and they are both very close to the analytical solutions even if a very coarse mesh, such as Mesh-2, is used. Similarly, contour of the stress field for Quad-P is the smoothest, as shown in Fig. 12(a)–(e).

6.4. Cook's skew beam

In this section, Cook's skew beam is considered, which is proposed by Cook et al. [45] to assess the ability of distortion with different types of elements. The material parameters and dimensions are shown in Fig. 13. A shear force of $F = 1$ is uniformly distributed on the right end of the beam and the left end is completely fixed. Reference solutions of major principal stress at point *B*, minor principal stress at point *C* and vertical displacement at point *A* are 0.2362, −0.2023 and 23.96 respectively, which are computed by the GT9M element with 64 × 64 mesh [46,47]. The results are listed in Tables 5–7 respectively. Quad-P has reached very high precision when mesh density is not very high, such as Mesh-4 and is linearly independent.

6.5. Earth slope

In this test, a homogeneous earth slope acted by self-weight is considered, as shown in Fig. 14. The bottom boundary is completely fixed and the normal constraints are imposed on both the left and right boundaries. The material is assumed as elastic with Young's modulus $E = 8 \times 10^7$, Poisson ratio $v = 0.43$ and unit weight $\gamma = 1.962 \times 10^4$. Due to the lack of theoretical solution, the slope model adopts a very fine mesh with 12,255 elements and 12,528

Table 10
Stress intensity factor M_I for the edge crack under tensile load.

Element type	Mesh types	Mesh-9	Mesh-15	Mesh-21	Mesh-27	Mesh-33
T3-0	DOFs	270	564	1090	1654	2380
	M_I	0.8344	0.8984	0.9318	0.9426	0.9540
T3-1	DOFs	746	1628	3206	4898	7076
	M_I	0.9908	0.9937	0.9953	0.9966	0.9969
Quad-0	DOFs	292	566	1092	1660	2382
	M_I	0.8750	0.9245	0.9471	0.9598	0.9672
Quad-1	DOFs	812	1634	3212	4916	7082
	M_I	0.9963	0.9978	0.9984	0.9985	0.9986
Quad-P	DOFs	812	1634	3212	4916	7082
	M_I	0.9934	0.9931	0.9958	0.9971	0.9978
	RD	0	0	0	0	0

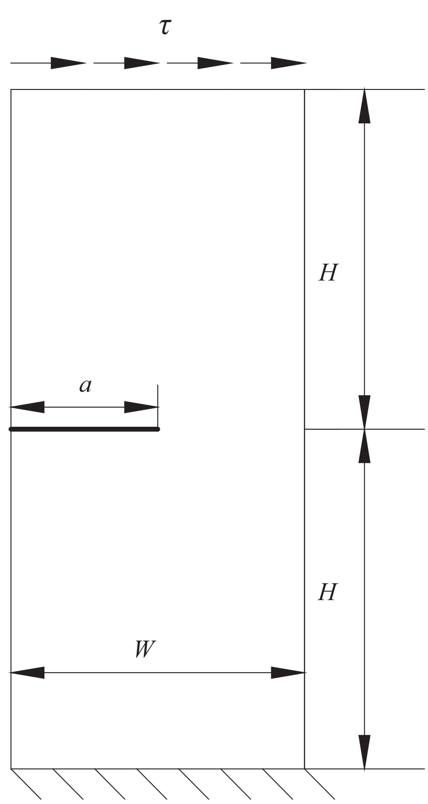

Fig. 16. A finite plate with an edge crack subjected to a uniform shear force.

nodes. A reference solution is calculated by four-node isoparametric quadrilateral element using this fined mesh. The reference solution for the horizontal displacement of point B and the vertical displacement of point A are −0.4209 and −1.6068 respectively [48]. The numerical results are shown in Tables 8 and 9 respectively. Obviously, nearly the same precision as above is observed.

6.6. An edge crack under tensile load

In this example, a finite rectangular plate with an edge crack subjected to a uniform tensile force $\sigma = 1.0$ on the top of the plate is discussed. The geometry of the test specimen is schematically depicted in Fig. 15. The geometric parameters are set as follows: height $2H = 6$, width $W = 2.0$, and crack length $a = 1.0$. The reference solution is given by Ewalds and Wanhill [49]

$$K_I = C\sigma\sqrt{a\pi}, \tag{65}$$

where C is the correction factor related with the size of the plate, and it can be represented as follows when $a/W \leqslant 0.6$

$$C = 1.12 - 0.231\left(\frac{a}{W}\right) + 10.55\left(\frac{a}{W}\right)^2 - 21.72\left(\frac{a}{W}\right)^3 + 30.39\left(\frac{a}{W}\right)^4. \tag{66}$$

As shown in Table 10, for T3-0 and Quad-0, they still have the errors of 4.6% and 3.28% respectively even if the finest mesh, Mesh-33, is used, while other meshes have a very high precision even when the mesh density takes the minimum value of 9. Simi-

Table 11
Stress intensity factors M_I for the edge crack under shear force.

Element type	Mesh types	Mesh-9	Mesh-15	Mesh-21	Mesh-27	Mesh-33
T3-0	DOFs	328	692	1266	2064	2952
	M_I	0.8491	0.9024	0.9367	0.9555	0.9678
T3-1	DOFs	920	2012	3734	6128	8792
	M_I	0.9953	0.9974	0.9981	0.9992	0.9994
Quad-0	DOFs	332	724	1308	2068	2956
	M_I	0.8862	0.9365	0.9579	0.9697	0.9794
Quad-1	DOFs	932	2108	3860	6140	8804
	M_I	0.9992	1.0000	1.0002	1.0004	1.0008
Quad-P	DOFs	932	2108	3860	6140	8804
	M_I	0.9941	0.9976	0.9994	0.9952	0.9974
	RD	0	0	0	0	0

Table 12
Stress intensity factors M_{II} for the edge crack under shear force.

Element type	Mesh types				
	Mesh-9	Mesh-15	Mesh-21	Mesh-27	Mesh-33
T3-0	0.9951	0.9685	0.9718	0.9632	0.9467
T3-1	1.0007	0.9997	1.0018	0.9928	0.9922
Quad-0	0.9938	1.0008	1.0045	1.0057	1.0068
Quad-1	0.9992	0.9989	0.9993	0.9982	0.9969
Quad-P	1.0039	0.9955	1.0069	0.9923	0.9935

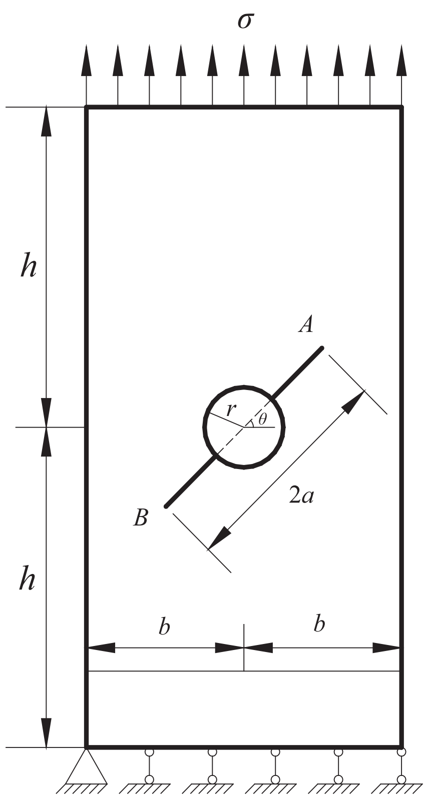

Fig. 17. Two cracks emanating from a circular hole.

larly, both Quad-1 and Quad-P have high precisions. While RD of the latter is 0, so it is still linearly independent even for the linear elastic fracture problems.

6.7. An edge crack under shear force

In this case, a mixed-mode crack is analyzed. Similarly, there is a finite rectangular plate with an edge crack but subjected to a uniform shear force $\tau = 1.0$ on the top of the plate, as shown in Fig. 16. The bottom boundary is completely fixed. The geometric parameters are as follows: height $2H = 16$, width $W = 7.0$, and crack length $a = 1.0$. The analytical solutions [3] of the mixed-mode SIFs for this case are $K_I = 34.0$ and $K_{II} = 4.55$.

The same conclusions can be made for the mixed-mode crack according to the numerical results in Tables 11 and 12.

6.8. Two cracks emanating from a circular hole

A finite plate with two cracks emanating from a hole subjected to a uniform tensile force $\sigma = 1.0$ is investigated in this section, as shown in Fig. 17. The following dimensions are taken: width $2b = 2$, height $2h = 4$ and hole radius $r = 0.25$. The reference solutions can be found in Ref. [50].

Comparisons of K_I and K_{II} at tip A when $a = 0.7$ and $\theta = 45^\circ$ are shown in Tables 13 and 14. Similarly, both Quad-1 and Quad-P have high precisions and the latter is linearly independent. For different combinations of a and θ, the results by Quad-P are shown in Tables 15 and 16. The maximum error is within 1%. High precision is verified again.

Table 13
Stress intensity factors M_I at crack tip A for the crack from a circular hole.

Element type	Mesh types					
		Mesh-9	Mesh-15	Mesh-21	Mesh-27	Mesh-33
T3-0	DOFs	392	848	1596	2364	3428
	M_{II}	0.9728	0.9896	0.9713	0.9790	0.9815
T3-1	DOFs	1064	2432	4676	6980	10,172
	M_{II}	1.0264	0.9915	0.9989	0.9977	0.9996
Quad-0	DOFs	432	848	1660	2468	3404
	M_{II}	0.9659	0.9683	0.9827	0.9946	0.9927
Quad-1	DOFs	1168	2416	4852	7276	10,084
	M_{II}	1.0114	1.0072	1.0009	1.0007	1.0004
Quad-P	DOFs	1168	2416	4852	7276	10,084
	M_{II}	0.9989	1.0062	0.9990	0.9984	0.9981
	RD	0	0	0	0	0

Table 14
Stress intensity factors M_{II} at crack tip A for the crack from a circular hole.

Element type	Mesh types				
	Mesh-9	Mesh-15	Mesh-21	Mesh-27	Mesh-33
T3-0	0.9841	0.9768	0.9970	0.9956	0.9978
T3-1	1.0086	0.9938	0.9993	1.0043	0.9995
Quad-0	0.9854	0.9943	0.9901	0.9904	0.9908
Quad-1	1.0025	1.0010	1.0001	1.0015	1.0011
Quad-P	0.9900	1.0046	1.0032	1.0029	1.0026

Table 15
Stress intensity factors at crack tip *A* for different parameter combinations.

θ		0.5	0.6	0.7	0.8
0°	DOFs	9790	9814	9838	9886
	M_I	1.0001	1.0008	1.0002	1.0031
	M_{II}	–	–	–	–
	RD	0	0	0	0
15°	DOFs	9814	9862	9886	6958
	M_I	1.0024	0.9993	0.9979	1.0075
	M_{II}	0.9993	0.9929	0.9942	1.0052
	RD	0	0	0	0
30°	DOFs	12,904	9886	9934	9958
	M_I	0.9985	0.9974	0.9985	0.9969
	M_{II}	0.9940	0.9984	0.9910	0.9966
	RD	0	0	0	0
45°	DOFs	9838	9886	9934	9982
	M_I	1.0007	0.9991	0.9981	0.9990
	M_{II}	0.9956	0.9978	1.0026	1.0009
	RD	0	0	0	0

Table 16
Stress intensity factors at crack tip *B* for different parameter combinations.

θ		0.5	0.6	0.7	0.8
0°	M_I	0.9974	1.0019	1.0060	0.9977
	M_{II}	–	–	–	–
15°	M_I	1.0020	0.9989	0.9972	1.0031
	M_{II}	1.0067	0.9913	1.0004	0.9999
30°	M_I	0.9970	0.9960	0.9966	0.9952
	M_{II}	1.0028	0.9990	0.9971	1.0005
45°	M_I	1.0056	0.9970	0.9960	0.9989
	M_{II}	1.0034	0.9939	0.9902	0.9997

7. Conclusions

With the same number of degrees of freedom as Quad-1, the proposed Quad-P has very high precision for both elastic problems and linear elastic fracture problems, but has no linear dependency issue. In addition, Quad-P is more advantageous than Quad-1 in the following aspects: the degrees of freedom of Quad-P are physically meaningful; stresses at nodes are continuous; the smoothing operation is no longer required in the post-processing process.

Acknowledgements

This study was supported by the National Natural Science Foundation of China under Grant Nos. 11502033, 51579016 and 51538001, the National Basic Research Program of China (973 Program) under Grant No. 2014CB047100, Fund of State Key Laboratory of Geomechanics and Geotechnical Engineering, Institute of Rock and Soil Mechanics, Chinese Academy of Sciences, Grant No. Z014010 and Special Project of Effective Development and Utilization of Water Resources, Grant No. 2016YFC0402008.

References

[1] Gerrard CM. Joint compliances as a basis for rock mass properties and the design of supports. Int J Rock Mech Min Sci Geomech Abstr 1982;19:285–305.
[2] Zheng H, Liu DF, Lee CF, Yue ZQ. A sophisticated node–pair model for interface problems. Comput Geotech 2004;31:137–53.
[3] Belytschko T, Black T. Elastic crack growth in finite elements with minimal remeshing. Int J Numer Meth Eng 1999;45:601–20.
[4] Strouboulis T, Babuška I, Copps K. The design and analysis of the generalized finite element method. Comput Meth Appl Mech Eng 2000;181:43–69.
[5] Bordas S, Moran B. Enriched finite elements and level sets for damage tolerance assessment of complex structures. Eng Fract Mech 2006;73(9):1176–201.
[6] Sukumar N, Moës N, Moran B, et al. Extended finite element method for three-dimensional crack modelling. Int J Numer Meth Eng 2000;48:1549–70.
[7] Areias P, Belytschko T. Analysis of three-dimensional crack initiation and propagation using the extended finite element method. Int J Numer Meth Eng 2005;63(5):760–88.
[8] Duddu R, Bordas SPA, Chopp D, et al. A combined extended finite element and level set method for biofilm growth. Int J Numer Meth Eng 2008;74(5):848–70.
[9] Liu GR, Dai KY, Nguyen TT. A smoothed finite element method for mechanics problems. Comput Mech 2007;39(6):859–77.
[10] Bordas S, Rabczuk T, Hung NX, et al. Strain smoothing in FEM and XFEM. Comput Struct 2010;88(23):1419–43.
[11] Vu-Bac N, Nguyen-Xuan H, Chen L, et al. A Node-Based Smoothed eXtended Finite Element Method (NS-XFEM) for fracture analysis. Comput Model Eng Sci 2011;73(4):331–56.
[12] Bordas S, Natarajan S, Kerfriden P, et al. On the performance of strain smoothing for quadratic and enriched finite element approximations (XFEM/GFEM/PUFEM). Int J Numer Meth Eng 2011;86(4–5):637–66.
[13] Chen L, Rabczuk T, Bordas S, et al. Extended finite element method with edge-based strain smoothing (ESm-XFEM) for linear elastic crack growth. Comput Meth Appl Mech Eng 2012;209:250–65.
[14] Natarajan S, Song C. Representation of singular fields without asymptotic enrichment in the extended finite element method. Int J Numer Meth Eng 2013;96(13):813–41.
[15] Nguyen-Xuan H, Liu GR, Bordas S, et al. An adaptive singular ES-FEM for mechanics problems with singular field of arbitrary order. Comput Meth Appl Mech Eng 2013;253:252–73.
[16] Nguyen VP, Anitescu C, Bordas S, et al. Isogeometric analysis: an overview and computer implementation aspects. Math Comput Simul 2015;117:89–116.
[17] Jing L. A review of techniques, advances and outstanding issues in numerical modelling for rock mechanics and rock engineering. Int J Rock Mech Min Sci 2003;40(3):283–353.
[18] Duarte CA, Hamzeh ON, Liszka TJ, et al. A generalized finite element method for the simulation of three-dimensional dynamic crack propagation. Comput Meth Appl Mech Eng 2001;190:2227–62.
[19] Duarte CA, Reno LG, Simone A. A high-order generalized FEM for through-the-thickness branched cracks. Int J Numer Meth Eng 2007;72:325–51.
[20] Belytschko T, Gu L, Lu YY. Fracture and crack growth by element free Galerkin methods. Model Simul Mater Sci Eng 1994;2:519–34.
[21] Rabczuk T, Bordas S, Zi G. A three-dimensional meshfree method for continuous multiple-crack initiation, propagation and junction in statics and dynamics. Comput Mech 2007;40(3):473–95.

[22] Rabczuk T, Zi G, Bordas S, et al. A geometrically non-linear three-dimensional cohesive crack method for reinforced concrete structures. Eng Fract Mech 2008;75(16):4740–58.
[23] Bordas S, Rabczuk T, Zi G. Three-dimensional crack initiation, propagation, branching and junction in non-linear materials by an extended meshfree method without asymptotic enrichment. Eng Fract Mech 2008;75(5):943–60.
[24] Rabczuk T, Zi G, Bordas S, et al. A simple and robust three-dimensional cracking-particle method without enrichment. Comput Meth Appl Mech Eng 2010;199(37):2437–55.
[25] Rabczuk T, Bordas S, Zi G. On three-dimensional modelling of crack growth using partition of unity methods. Comput Struct 2010;88(23):1391–411.
[26] Nguyen VP, Rabczuk T, Bordas S, et al. Meshless methods: a review and computer implementation aspects. Math Comput Simul 2008;79(3):763–813.
[27] Cundall PA. A computer model for simulating progressive, large scale movements in blocky rock systems. In: Proceedings of the international symposium rock fracture, vol. 1. ISRM, Nancy, Paper No II-8 ; 1971.
[28] Shi GH, Goodman RE. Two dimensional discontinuous deformation analysis. Int J Numer Anal Meth Geomech 1985;9:541–56.
[29] Camones LAM, do Amaral Vargas E, de Figueiredo RP, et al. Application of the discrete element method for modeling of rock crack propagation and coalescence in the step-path failure mechanism. Eng Geol 2013;153:80–94.
[30] Ning Y, Yang J, Ma G, et al. Modelling rock blasting considering explosion gas penetration using discontinuous deformation analysis. Rock Mech Rock Eng 2011;44:483–90.
[31] Shi GH. Manifold method of material analysis. In: Transactions of the ninth army conference on applied mathematics and computing, Minneapolis, Minnesota, USA. p. 51–76.
[32] Zheng H, Liu ZJ, Ge XR. Numerical manifold space of Hermitian form and application to Kirchhoff's thin plate problems. Int J Numer Meth Eng 2013;95:721–39.
[33] Wu Z, Wong LNY. Frictional crack initiation and propagation analysis using the numerical manifold method. Comput Geotech 2012;39:38–53.
[34] Zheng H, Xu D. New strategies for some issues of numerical manifold method in simulation of crack propagation. Int J Numer Meth Eng 2014;97:986–1010.
[35] Zheng H, Liu F, Li CG. The MLS-based numerical manifold method with applications to crack analysis. Int J Fract 2014;190:47–166.
[36] Ma GW, An XM, Zhang HH, et al. Modeling complex crack problems using the numerical manifold method. Int J Fract 2009;156:21–35.
[37] Ning YJ, An XM, Ma GW. Footwall slope stability analysis with the numerical manifold method. Int J Rock Mech Min Sci 2011;48:964–75.
[38] An XM, Li LX, Ma GW, et al. Prediction of rank deficiency in partition of unity-based methods with plane triangular or quadrilateral meshes. Comput Meth Appl Mech Eng 2011;200:665–74.
[39] Zienkiewicz OC, Taylor RL. The finite element method: solid mechanics (Volume 2) [M]. Butterworth-Heinemann; 2000. p. 124–7.
[40] Kang Z, Bul TQ, Nguyen DD, et al. An extended consecutive-interpolation quadrilateral element (XCQ4) applied to linear elastic fracture mechanic. Acta Mech 2015. doi: http://dx.doi.org/10.1007/s00707-015-1451-y.
[41] Peng X, Kulasegaram S, Bordas SPA, et al. An extended finite element method with smooth nodal stress; 2013. p. 1–46. Available from: arXiv: 1306.0536.
[42] Moës N, Dolbow J, Belytschko T. A finite element method for crack growth without remeshing. Int J Numer Meth Eng 1999;46(1):131–50.
[43] Augarde CE, Deeks AJ. The use of Timoshenko's exact solution for a cantilever beam in adaptive analysis. Finite Elem Anal Des 2008;44(9):595–601.
[44] Timoshenko SP, Goodier JN. Theory of elasticity. 3rd ed. New York: McGraw-Hill; 1970.
[45] Cook RD, Malkus DS, Plesha ME. Concepts and applications of finite element analysis. 3rd ed. New York: John Wiley; 1989.
[46] Long Y, Xu Y. Generalized conforming triangular membrane element with vertex rigid rotational freedoms. Finite Elem Anal Des 1994;17(4):259–71.
[47] Fu XR, Cen S, Li CF, et al. Analytical trial function method for development of new 8-node plane element based on the variational principle containing Airy stress function. Eng Comput 2010;27(4):442–63.
[48] Yang Y, Bi R, Zheng H. A hybrid 'FE-Meshless' QUAD4 with continuous nodal stress using radial-polynomial basis functions. Eng Anal Boundary Elem 2015;53:73–85.
[49] Ewalds H, Wanhill R. Fracture mechanics. New York: Edward Arnold; 1989.
[50] Chinese Aeronautical Establishment. Handbook of the stress intensity factor. revised ed. Beijing: Science Press; 1993.